

Motion of a rigid particle in the lid-driven cavity flow

Fan Yang(杨帆), Zhe Yan(闫喆), Wencan Wang(汪文灿), and Ren Shi(施任)

Citation: Chin. Phys. B, 2025, 34 (**3**): 034701. DOI: 10.1088/1674-1056/ada438
Journal homepage: http://cpb.iphy.ac.cn; http://iopscience.iop.org/cpb

What follows is a list of articles you may be interested in

On the spreading behavior of a droplet on a circular cylinder using the lattice Boltzmann method

Fan Yang(杨帆), Hu Jin(金虎), and Mengyao Dai(戴梦瑶)
Chin. Phys. B, 2024, 33 (**6**): 064702. DOI: 10.1088/1674-1056/ad3b7f

Morphological analysis for thermodynamics of cavitation collapse near fractal solid wall

Minglei Shan(单鸣雷), Yu Yang(杨雨), Xuefen Kan(阚雪芬), Cheng Yin(殷澄), and Qingbang Han(韩庆邦)
Chin. Phys. B, 2024, 33 (**6**): 064701. DOI: 10.1088/1674-1056/ad3343

Simulation of gas-liquid two-phase flow in a flow-focusing microchannel with the lattice Boltzmann method

Kai Feng(冯凯), Gang Yang(杨刚), and Huichen Zhang(张会臣)
Chin. Phys. B, 2023, 32 (**11**): 114703. DOI: 10.1088/1674-1056/acea6e

Effect of viscosity on stability and accuracy of the two-component lattice Boltzmann method with a multiple-relaxation-time collision operator investigated by the acoustic attenuation model

Le Bai(柏乐), Ming-Lei Shan(单鸣雷), Yu Yang(杨雨), Na-Na Su(苏娜娜), Jia-Wen Qian(钱佳文), and Qing-Bang Han(韩庆邦)
Chin. Phys. B, 2022, 31 (**3**): 034701. DOI: 10.1088/1674-1056/ac2b93

Three-dimensional turbulent flow over cube-obstacles

Hao Lu(卢浩), Wen-Jun Zhao(赵文君), Hui-Qiang Zhang(张会强), Bing Wang(王兵), Xi-Lin Wang(王希麟)
Chin. Phys. B, 2017, 26 (**1**): 014703. DOI: 10.1088/1674-1056/26/1/014703

Motion of a rigid particle in the lid-driven cavity flow

Fan Yang(杨帆)[1,2,†], Zhe Yan(闫喆)[1], Wencan Wang(汪文灿)[1], and Ren Shi(施任)[1]

[1] *School of Energy and Power Engineering, University of Shanghai for Science and Technology, Shanghai* 200093, *China*
[2] *Shanghai Key Laboratory of Multiphase Flow and Heat Transfer in Power Engineering, Shanghai* 200093, *China*

(Received 1 November 2024; revised manuscript received 7 December 2024; accepted manuscript online 31 December 2024)

The motion of an elliptical rigid particle in a lid-driven cavity flow was numerically simulated using the immersed boundary lattice Boltzmann method (IB-LBM). The effects of the particle's initial orientation angle, initial position, aspect ratio, and size on the motion characteristics were investigated. The computational results indicate that the particle's motion undergoes two distinct stages: a starting stage that involves moving from the release position to a limit cycle, and a periodic stage that involves moving on the limit cycle. The initial orientation of the particle has a minimal impact on both stages of motion. In contrast, the time it takes for the particle to reach the limit cycle may vary depending on the release position. Furthermore, particles with a larger aspect ratio exhibit a greater maximum velocity magnitude; an increase in particle size causes the particle trajectory to contract more toward the center of the cavity, decreasing the centrifugal force experienced by the particle.

Keywords: lattice Boltzmann methods, immersed boundary method, elliptical rigid particle, lid-driven cavity flow

PACS: 47.11.Qr, 47.61.Jd, 47.55.Kf

DOI: 10.1088/1674-1056/ada438 **CSTR:** 32038.14.CPB.ada438

1. Introduction

Particle-laden flows are ubiquitous in industrial processes and scientific researches, such as the flow of red blood cells in the blood,[1] the separation of cancer cells through microfluidic vortices,[2] particle separation and transport in microfluidic chips,[3] and the transportation of porous particles in oil wells.[4] The study of particle dynamics within enclosed geometric spaces has long been a research hotspot due to its significance in practical applications and theoretical research.[5,6] The lid-driven cavity flow, as a classical case in computational fluid dynamics, not only provides a theoretical basis for simulating complex engineering problems such as mixing processes in chemical reactors and heat exchanger design but also constructs a controllable experimental environment, facilitating researchers to delve into the interaction mechanisms between fluid and particles.[7–9] This flow pattern has become an important benchmark for researchers to understand and predict particle behaviors in complex flow fields because it can exhibit key fluid dynamic issues such as vortex formation, turbulence characteristics, and fluid-driven particle motion.

Over the past decades, numerous researchers have employed various numerical and experimental techniques to study the behavior of rigid particles in lid-driven cavity flows. Tsorng *et al.*[10] combined three-dimensional imaging and signal processing techniques to demonstrate the three-dimensional trajectories of individual particles within the cavity, obtaining characteristics of particle trajectory distribution and the phenomenon of particles tending to aggregate along specific paths. Kosinski *et al.*[5] used the Euler–Lagrange method to study the behavior of circular particles dragged by the lid-driven fluid at a Reynolds number of 1000, showing that particles tend to migrate towards the wall, and the higher the Stokes number, the stronger the migration process towards the wall. Puragliesi *et al.*[11] conducted a numerical simulation of natural convection with vertical heating of air in a square cavity at high Rayleigh numbers using the direct numerical simulation (DNS) method, discussing the role of the mean pressure field in natural convection under stable stratification conditions and analyzing the factors affecting particle sedimentation.

The lattice Boltzmann method (LBM), as an emerging computational fluid dynamics technique in recent years, has increasingly gained attention due to its unique advantages in dealing with complex flow problems. This method, with its efficiency and flexibility in multi-scale and multi-physical process simulations, provides a powerful tool for in-depth exploration of the intrinsic mechanisms of fluid flow.[12,13] Therefore, it has been widely applied to fields such as particle suspension,[14] cavitation flow,[15] natural convection,[16] mass transfer and other fields.[17,18]

For lid-driven cavity flows, Hu *et al.*[19,20] used the LBM to study the motion of neutrally buoyant circular particles in single-sided and double-sided driven square cavities respectively. The results revealed that in single-sided driven square cavities, the motion of particles is characterized by the exis-

[†]Corresponding author. E-mail: usstyf@126.com

© 2025 Chinese Physical Society and IOP Publishing Ltd. All rights, including for text and data mining, AI training, and similar technologies, are reserved.

tence of a limit cycle, which is independent of the initial position of the particles, and the limit cycle changes with the increase of Reynolds number; in double-sided driven square cavities, the motion of particles in the cavity eventually stabilizes on the limit cycle, and the limit cycle is compressed along the diagonal with the increase of Reynolds number. Zhang *et al.*[21] used the LBM to numerically study the motion of two-dimensional circular neutrally buoyant particles in a double-lid driven cavity with thermal flow, examining the effects of the cavity's Grashof number (*Gr*) and Reynolds number (*Re*) on particle motion within a certain numerical range. It was found that the motion of particles in the cavity flow exhibits four different modes, and a relationship diagram between the particle motion modes and *Gr* as well as *Re* was further obtained. Wang *et al.*[22] used a modified slip boundary format of the LBM to study the motion of neutrally buoyant circular slipping particles in a clockwise double-lid driven square cavity, demonstrating the effects of slip length, initial particle position, Reynolds number, and particle diameter on the migration of slipping particles.

Despite the significant progress made in the study of rigid neutrally buoyant particles in lid-driven cavity flows, traditional methods still face challenges such as high grid generation costs and computational difficulties when dealing with the dynamic boundary fluid–solid coupling problem of particle motion. To avoid the computational cost of regenerating grids, Ladd proposed the shell model,[23] assuming that the fluid can fill the entire flow field (i.e., inside and outside the particles), and the particle wall is represented by grid midpoints. The fluid forces and torques acting on the particles are calculated using the momentum exchange method, successfully simulating the sedimentation problem of particle groups. Mei *et al.*[24] proposed an improved refilling algorithm that can construct a pressure field consistent with the known velocity field and successfully applied it to the problem of forced oscillation of cylinders. Inamuro *et al.*[25] used the LBM based on the stress integration method to study the inertial migration of neutral particles in Poiseuille flow and successfully reproduced the Segre–Silberberg effect. Francesco and Hendrik[26] used the discontinuous Galerkin finite element method to study the motion of circular particles in a square cavity and studied the effects of particle radius and particle-fluid density ratio on the particle–boundary interaction. Gan *et al.*[27] used the finite element method to solve fluid–solid coupling equations and combined the arbitrary Lagrangian–Eulerian (ALE) method to study the sedimentation problem of particles in thermal convection at moderate Reynolds number, and under isothermal conditions, pointing out that the variation of the DKT phenomenon depends on *Re* and the width of the square cavity. Yu *et al.*[28] used the distributed Lagrange multiplier/fictitious domain method to simulate the sedimentation problem of single particles and extended it to the case where the particle boundary temperature changes. Feng *et al.*[29,30] used the finite difference coupled immersed boundary method (IBM) method to well reproduce the simulation results of Yu.[28]

Among the various methods for dealing with fluid–solid coupling problems such as particle motion, IBM can handle complex geometries without the need for body-fitted grids. It simulates fluid dynamics on a fixed Eulerian grid while considering the motion of rigid or flexible structures embedded in the fluid. The flexibility and applicability of this method make it an ideal choice for exploring the behavior of particles in enclosed space flows. Since Peskin[31] proposed IBM in the 1970s, many scholars have innovated and improved it on this basis and carried out a series of research work. Feng and Michaelides[32] combined IBM and the LBM, successfully achieving no-slip conditions for moving particle boundaries in high Reynolds number fluids by introducing a driving term in the momentum equation. Shin and Sung[33] studied the inertial migration of elastic particles in two-dimensional Poiseuille flow based on IB-LBM, revealing the different focusing characteristics of particles under different *Re*. Sun *et al.*[34] used IB-LBM to study the focusing phenomenon of single and multiple particles in straight microchannels, pointing out that the equilibrium position of particle focusing is related to particle size and *Re* number. Chen *et al.*[35] established a three-dimensional particle model in Poiseuille flow through the IB-LBM method, finding that the migration of soft particles from the channel wall to the channel center depends on particle inertia and deformation degree, while the stable state of hard particles is independent of shear rate. Kim *et al.*[36] established an elastic particle model in Poiseuille flow using the IB-LBM method, observing three dynamics of particle tank tread motion, rotation, and tumbling, and believing that the final equilibrium position of particles depends on the action of wall and shear gradient. Mukundakrishnan *et al.*[37] used the IB-LBM method to study the motion of two spherical particles in confined rotating flow, pointing out that the motion morphology of particles is significantly affected by particle–particle and particle–wall interaction forces. Eshghinejadfard and Thevenin[38] extended IB-LBM to three-dimensional particle group sedimentation, considering the cases of fixed and variable particle temperatures, to study the effect of heat transfer on the motion of spherical catalyst particles. Zhang *et al.*[39] used IB-LBM coupled with the discrete element method (DEM) to compare Dirichlet boundary conditions and Neumann boundary conditions and studied the effect of Neumann boundary conditions on particle motion in thermal fluids.

From the current literature, it can be seen that although particle flow research based on the immersed boundary method has gained certain results, there are still fewer studies

on non-circular particles in lid-driven flows.[40] In this paper, IB-LBM is used to study the motion of an elliptical particle in lid-driven flow. The organization of this paper is as follows. First, a brief introduction to LBM and IBM is given. Then, a classic flow problem is simulated to meticulously verify the computational code, ensuring its effectiveness and accuracy in subsequent simulations. Then, the motion characteristics of a neutrally buoyant elliptical particle in lid-driven square cavity are explored in depth. Multiple key factors affecting particle motion are analyzed in detail, including initial orientation angle, initial position, particle aspect ratio, and particle size. At the end of the paper, the research results are comprehensively sorted out, and several conclusions are drawn.

2. Mathematical models

2.1. Multiple relaxation time lattice Boltzmann method (MRT-LBM)

The MRT-LBM model proposed by Guo and Zheng[41] is employed, and its evolution equation is as follows:

$$\begin{aligned} & f_i(\boldsymbol{x}+\boldsymbol{e}_i\delta_t, t+\delta_t) - f_i(\boldsymbol{x},t) \\ = & -\boldsymbol{M}^{-1}\boldsymbol{S}(\boldsymbol{m}-\boldsymbol{m}^{\mathrm{eq}}) + \boldsymbol{M}^{-1}\boldsymbol{M}F_i\delta_t, \end{aligned} \tag{1}$$

where $\boldsymbol{S} = \mathrm{diag}(0, s_e, s_\varepsilon, 0, s_q, 0, s_q, s_\nu, s_\nu)$ is the relaxation matrix.[32] For the equilibrium distribution function $f_i^{\mathrm{eq}}(\boldsymbol{x},t)$, the He–Luo model[42] is used:

$$f_i^{\mathrm{eq}} = \omega_i \left[\rho_0 + \rho \left(\frac{\boldsymbol{e}_i \cdot \boldsymbol{u}}{c_s^2} + \frac{(\boldsymbol{e}_i \cdot \boldsymbol{u})^2}{2c_s^4} - \frac{\boldsymbol{u}^2}{2c_s^2} \right) \right]. \tag{2}$$

Unlike the SRT-LBE where the collision step is performed in the velocity space $\boldsymbol{f} = f_k$, $k = 0, 1, \ldots, 8$,[43] in MRT-LBE, the collision step is executed in the moment space $\boldsymbol{m} = m_k$, $k = 0, 1, \ldots, 8$. The relationship between $\boldsymbol{f}$ and $\boldsymbol{m}$ is given by

$$\boldsymbol{m} = \boldsymbol{M}\boldsymbol{f}, \quad \boldsymbol{m}^{\mathrm{eq}} = \boldsymbol{M}\boldsymbol{f}^{\mathrm{eq}}. \tag{3}$$

The macroscopic quantities are calculated using the following formulas:

$$\rho = \sum_{i=0}^{8} f_i, \tag{4}$$

$$\boldsymbol{u}^* = \frac{\sum_{i=0}^{8} \boldsymbol{e}_i f_i}{\rho}, \tag{5}$$

$$\boldsymbol{u} = \boldsymbol{u}^* + \frac{1}{2\rho}\boldsymbol{f}(\boldsymbol{x},t)\delta_t, \tag{6}$$

where $\boldsymbol{f}(\boldsymbol{x},t)$ is the external force term in the flow field, $p = \rho c_s^2$ is the fluid pressure, and $\nu = (\tau - 0.5)c_s^2\delta_t$ is the kinematic viscosity.

The F_i is a discrete external force distribution function in Eq. (1) and can be obtained from the volume force $\boldsymbol{f}(\boldsymbol{x},t)$ acting on the fluid and the velocity $\boldsymbol{u}$:

$$F_i = \left(1 - \frac{1}{2\tau}\right) \omega_i \left(\frac{e_i - \boldsymbol{u}}{c_s^2} + \frac{e_i \cdot \boldsymbol{u}}{c_s^4} \cdot \boldsymbol{e}_i \right) \boldsymbol{f}(x,t). \tag{7}$$

2.2. Direct force immersed boundary-lattice Boltzmann method (DF-IB-LBM)

In the IB-LBM, the fluid cells are described by a fixed Eulerian grid $\boldsymbol{x} = \boldsymbol{x}(x,y)$, and the solid boundaries are represented by a set of ordered, movable Lagrangian points $\boldsymbol{X} = \boldsymbol{X}(X,Y)$. This paper adopts the DF-IBM proposed by Kang and Hassan,[44] which is simple to implement and computationally efficient.

In the DF-IBM, the interpolation of velocity and the propagation of force are illustrated in Fig. 1, where $\boldsymbol{F}_{\mathrm{f}}$, $\boldsymbol{F}_{\mathrm{t}}$, and $\boldsymbol{F}_{\mathrm{n}}$ represent the force vector at the m-th Lagrangian point $\boldsymbol{X}_m$, and its tangential and normal components, respectively. The calculation formula for $\boldsymbol{F}_{\mathrm{f}}$ is given by

$$\boldsymbol{F}_{\mathrm{f}}(\boldsymbol{X}_m,t) = \frac{2\rho_{\mathrm{l}}(\boldsymbol{X}_m,t)}{\delta_t} \left(\boldsymbol{U}^{\mathrm{d}}(\boldsymbol{X}_m,t) - \boldsymbol{U}^*(\boldsymbol{X}_m,t) \right), \tag{8}$$

where $\boldsymbol{U}^{\mathrm{d}}$ is the self-propelled velocity of the Lagrangian point, $\boldsymbol{U}^*$ is the intermediate velocity of the fluid at the Lagrangian point without external forces, $\rho_{\mathrm{l}}(\boldsymbol{X}_m,t)$ is the fluid density at the Lagrangian point, and $\rho_{\mathrm{l}}(\boldsymbol{X}_m,t)$ and $\boldsymbol{U}^*$ can be interpolated from the nearby Eulerian points using

$$\boldsymbol{U}^*(\boldsymbol{X}_m,t) = \sum_{i,j} \boldsymbol{u}^*(\boldsymbol{x}_{ij},t)\delta_h(\boldsymbol{x}_{ij} - \boldsymbol{X}_m)h^2, \tag{9}$$

$$\rho_{\mathrm{l}}(\boldsymbol{X}_m,t) = \sum_{i,j} \rho(\boldsymbol{x}_{ij},t)\delta_h(\boldsymbol{x}_{ij} - \boldsymbol{X}_m)h^2, \tag{10}$$

where $\boldsymbol{x}_{ij} = (x_i, y_j)$ represents the Eulerian grid points, h is the grid spacing between adjacent Eulerian grid points, and $\delta_h(\boldsymbol{x}_{ij} - \boldsymbol{X}_m)$ is the Dirac delta interpolation function, as shown in Fig. 1. Here, the following form proposed by Peskin[31] is used:

$$\delta_h(\boldsymbol{x}_{ij} - \boldsymbol{X}_m) = D(x_i - X_m)D(y_i - Y_m), \tag{11}$$

$$D(r) = \begin{cases} \dfrac{1}{8h}\left(3 - 2|\boldsymbol{r}|/h + \sqrt{1 + 4|\boldsymbol{r}|/h - 4(|\boldsymbol{r}|/h)^2}\right) & h \le |\boldsymbol{r}|, \\ \dfrac{1}{8h}\left(5 - 2|\boldsymbol{r}|/h + \sqrt{-7 + 12|\boldsymbol{r}|/h - 4(|\boldsymbol{r}|/h)^2}\right) & h \le |\boldsymbol{r}| \le 2h, \\ 0 & \text{otherwise}. \end{cases} \tag{12}$$

After solving for the boundary force density acting on the Lagrangian points, the force density at the boundary points $\boldsymbol{F}_{\rm f}(\boldsymbol{X}_m,t)$ can be distributed to the surrounding fluid Eulerian points using the following formula:

$$\boldsymbol{f}(\boldsymbol{x}_{ij},t)=\sum_{m=1}^{N_{\rm b}}\boldsymbol{F}_{\rm f}(\boldsymbol{X}_m,t)\delta_h(\boldsymbol{x}_{ij}-\boldsymbol{X}_m)h\Delta s, \tag{13}$$

where $N_{\rm b}$ is the total number of Lagrangian points, Δs represents the arc length between adjacent Lagrangian points, and the force $\boldsymbol{f}(\boldsymbol{x}_{ij},t)$ obtained by the Eulerian points is the external force term in Eqs. (6) and (7).

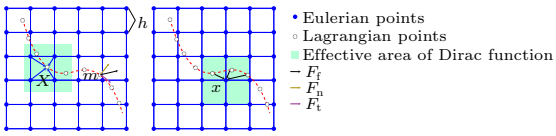


Fig. 1. Velocity interpolation (left) and force propagation (right).

3. Method verification

The effectiveness of the method employed in this study will be verified by simulating the DKT (drafting, kissing, tumbling) problem of two-dimensional circular particle sedimentation under the influence of gravity. At the initial moment, two circular particles are stationary in the channel with their relative positions shown in Fig. 2. As the two particles begin to sediment under the action of gravity, the leading particle gradually forms a low-pressure wake behind it. When the following particle enters the low-pressure wake of the leading particle, the fluid resistance it experiences decreases, causing an increase in velocity and gradual approach to the leading particle. Subsequently, the two particles collide and tumble, with the leading particle being pushed to one side and the following particle overtaking the leading particle. This is the so-called "DKT" phenomenon.

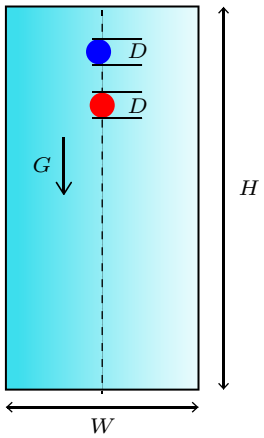


Fig. 2. Schematic diagram of sedimentation of two particles.

In this section, the computational domain is set to dimensions $W\times H=2$ cm$\times 8$ cm, with fluid viscosity $\nu=0.01$ g/(cm·s). It is assumed that the particles are perfectly rigid with a diameter $D=0.2$ cm. The initial coordinates of the particle centers are (0.999 cm, 7.2 cm) and (1.0 cm, 6.8 cm), respectively. The density ratio of the particles to the fluid is 1.01, and the gravitational acceleration $g=980$ cm/s^2. The motion of the particles adheres to Newton's laws of dynamics. To prevent overlap between particles and between particles and the wall, the Lennard–Jones potential function is used as a collision function, the specific formula of which can refer to the work of Niu *et al.*[45]

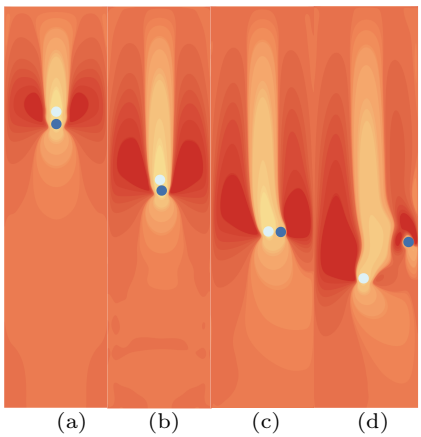


Fig. 3. Vertical velocity field of the fluid surrounding two particles at different moments: (a) $t=1.5$ s; (b) $t=2.5$ s; (a) $t=3.0$ s; (b) $t=4.5$ s.

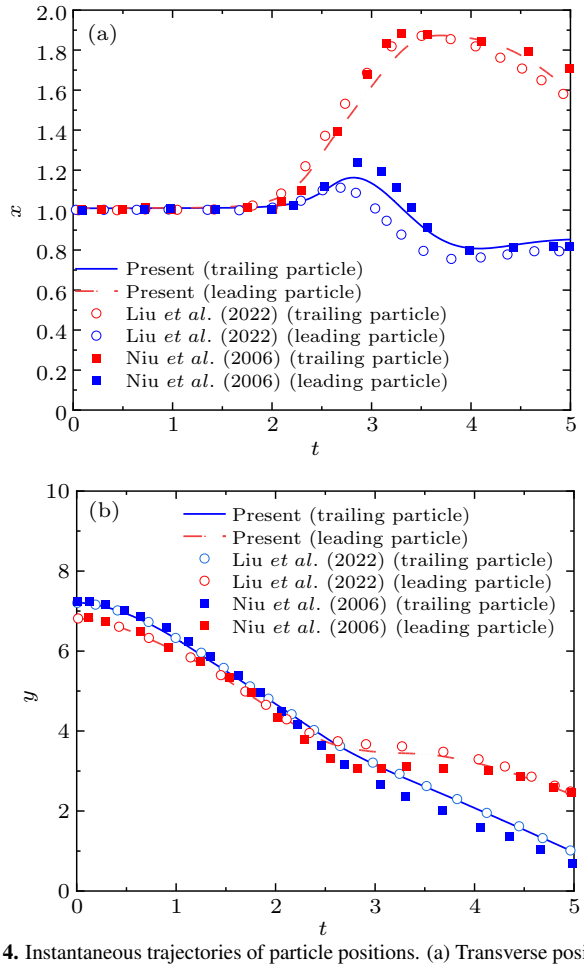


Fig. 4. Instantaneous trajectories of particle positions. (a) Transverse position instantaneous curves, (b) longitudinal position instantaneous curves.

Figure 3 illustrates the positions of the particles and the vertical velocity field of the surrounding fluid at several typical moments. It can be observed that initially, the two particles maintain a stable distance from each other. Subsequently, the following particle gradually approaches the leading particle until they come into contact with each other. After the tumbling process, the two particles deviate from the central line of the channel and eventually separate, with the DKT phenomenon being fully simulated. Figure 4 shows the instantaneous transverse and longitudinal coordinates of the particle centers calculated in this study, as well as those obtained by Niu *et al.*[45] and Liu *et al.*[46] It can be seen that the results of this study are in good agreement with the results reported in the literature.

4. Results and discussion

In this section, the rigid particles are initialized as elliptical, with the arc length $\Delta s = 0.6h$ between adjacent Lagrangian points on the particle boundary. The motion of the rigid particles in the lid-driven cavity flow is studied under different conditions. Figure 5 is a schematic diagram of the problem, where the side length of the square cavity is L, the upper boundary moves with a uniform velocity U, and the remaining boundaries are stationary solid walls. The Reynolds number in the cavity is defined as

$$Re = \frac{\rho \cdot U \cdot L}{\mu}, \tag{14}$$

where ρ is the fluid density and μ is the fluid dynamic viscosity.

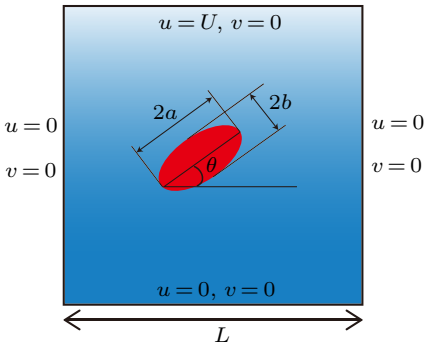


Fig. 5. Schematic diagram of elliptical particle in lid-driven cavity flow.

The elliptical particle is assumed to be a neutrally buoyant particle with a density equal to the surrounding flow field. The major axis length of the particle is $2a$, and the minor axis length is $2b$. The initial orientation angle is θ, and the mass of the particle is defined as

$$m_{\mathrm{P}} = \rho \cdot \pi \cdot a \cdot b. \tag{15}$$

The relative size of the particle is defined as

$$r = \frac{a}{L}. \tag{16}$$

The aspect ratio of the particle is defined as

$$\varphi = \frac{a}{b}. \tag{17}$$

During the movement of the particle, the dimensionless relative position of the particle is defined as

$$aL = \sqrt{(X_{\mathrm{P}} - 0.5L)^2 + (Y_{\mathrm{P}} - 0.5L)^2}, \tag{18}$$

where X_{P} and Y_{P} are the X and Y coordinates of the centroid of the elliptical particle, respectively.

The magnitude of dimensionless velocity of the particle is defined as

$$\bar{u} = \frac{|u|}{U}, \tag{19}$$

where $|u|$ represents the velocity magnitude of the centroid of the elliptical particle.

The dimensionless angular velocity of the particle is defined as

$$\bar{\omega} = \frac{\omega}{\pi}. \tag{20}$$

The total hydrodynamic force acting on the particle is defined as

$$\bar{M} = \sum_m \boldsymbol{F}_{\mathrm{f}} \times (\boldsymbol{X}_m - \boldsymbol{X}_{\mathrm{P}}). \tag{21}$$

The centrifugal force acting on the particle is defined as

$$F_{\mathrm{c}} = \frac{u^2 \cdot m_{\mathrm{P}}}{\sqrt{ab}}. \tag{22}$$

In the simulation, the dimensionless time is defined as

$$\tau = \frac{t \cdot U}{L}. \tag{23}$$

4.1. Motion of an elliptical particle

Under the traction of the lid-driven fluid, the elliptical particle will move within a square cavity, and the fluid flow will also be affected by the motion of the particle. Therefore, the motion of the particle will interact with the fluid flow. To understand the motion of the elliptical rigid particle and its interaction with the fluid, this study selects a grid resolution of $a = 25.6\Delta x$, where $\Delta x = \Delta y = 1$, the length of the square cavity is set to $L = 2a$, the velocity of the upper boundary is set to $U = 0.1$, the particle density is the same as the initial density of the flow field, set to 1.0, the Reynolds number of the background flow field is fixed at 1000, and the dynamic viscosity of the fluid is given by the relationship $\mu = \rho \cdot U \cdot L/Re$; the dimensionless relaxation time is determined by the relationship $\tau = 0.5 + \nu/c_s^2\Delta t$, where $c_s^2 = c^2/3 = (\Delta x/\Delta t)^2/3 = 1/3$. In this section, the particle size r is fixed at 0.05, the aspect ratio φ is fixed at 2, the initial orientation angle θ is 45°, and the initial release position is at $(0.25L, 0.25L)$. The rigid elliptical particle is released to observe its motion behavior within the square cavity.

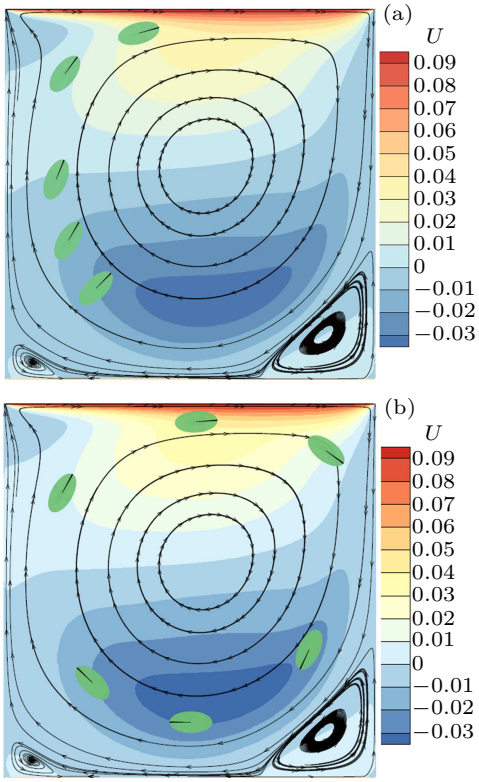


Fig. 6. Motion patterns at different stages of an elliptical particle in lid-driven cavity flow. (a) Starting stage, (b) periodic stage.

In the lid-driven cavity flow, the flow field forms a main vortex that rotates clockwise due to the uniform motion of the lid, creating a rotating fluid region at the center of the cavity. The intense swirling motion of this main vortex significantly affects the motion of particles. Outside the main vortex, due to the interaction between the fluid and the cavity walls, multiple secondary vortices are formed. Although these secondary vortices are not as extensive as the main vortex, they also influence the particle's direction and trajectory.

The motion of an elliptical particle in the lid-driven cavity flow can be divided into two stages. Figure 6(a) illustrates the starting stage of motion, where the particle is released from the lower left corner with an initial orientation angle of 45° and is immediately influenced by the main vortex, beginning to deflect counterclockwise along the direction of fluid motion. As the particle interacts with the fluid, it gradually adjusts its shape, tending to align its major axis parallel to the flow lines. Entering the periodic stage, as shown in Fig. 6(b), after the initial dynamic adjustment, the particle spontaneously changes direction and ultimately achieves parallelism between its major axis and the streamlines.

Figure 7(a) shows the trajectory of the particle's centroid, which, after the initial dynamic adjustment, eventually enters a stable motion state, forming and maintaining a limit cycle. This limit cycle represents the trajectory where the particle reaches a dynamic equilibrium in the flow field, and its formation is closely related to the vortex action in the lid-driven cavity flow. Figure 7(b) shows the instantaneous curves of the relative distance aL from the particle centroid to the cavity center, the dimensionless velocity $\bar{u}$, the magnitude of dimensionless hydrodynamic force $|\boldsymbol{F}|_{\mathrm{f}}$, the dimensionless angular velocity $\bar{\omega}$, and the dimensionless total hydrodynamic torque $\overline{M}$ acting on the particle since its release. The red vertical line corresponds to the specific moment when the particle's motion stage changes, which is defined as T^*. It can be observed that after entering the periodic stage, these physical quantities exhibit a clear periodicity. Calculations show that the motion period of the elliptical particle is approximately $T = 8.5$, which is consistent with previous studies on the motion characteristics of neutrally buoyant particles in cavity flow. This periodic phenomenon is due to the inertial drive, where the particle first undergoes centrifugal motion, moving away from the starting point, and then its motion is constrained by the square cavity, leading to a stable limit cycle.

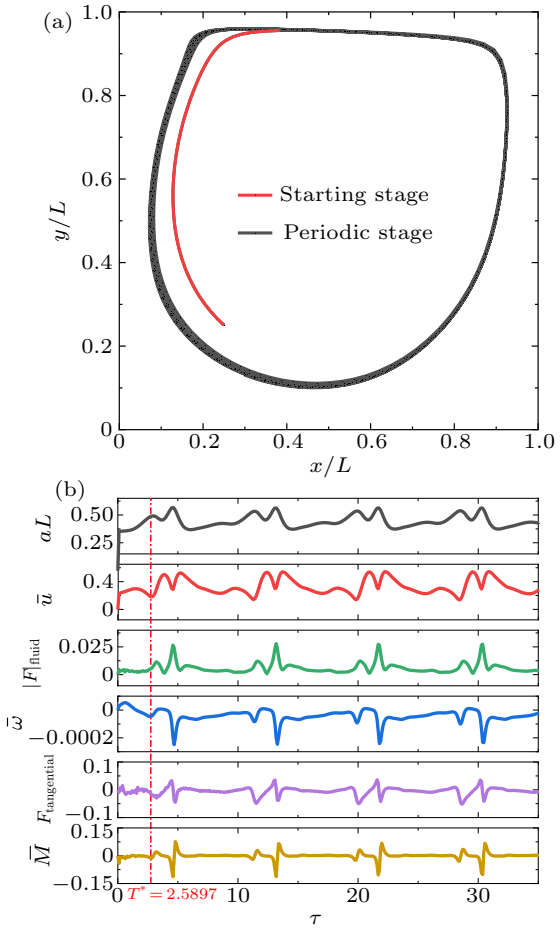


Fig. 7. Trajectory and instantaneous curves of physical parameters of an elliptical particle in lid-driven cavity flow. (a) Trajectory, (b) instantaneous curves of physical parameters.

To further discuss the cause of periodicity, a time period corresponding to one cycle within the periodic stage of particle motion, from $26 \leq \tau \leq 35$, is selected to show the time history of the particle's distance aL from the cavity center and the dimensionless velocity $\bar{u}$, as shown in Fig. 8(a). It can be seen that within one cycle, aL and $\bar{u}$ both have six extreme

values, denoted by letters A–B–C–D–E–F. The relative position of the particle in the cavity at each moment is shown in Fig. 8(b). From the figure, it can be observed that during the time interval $26.8967 \leq \tau \leq 28.6116$ (A–B segment), the particle moves upward along the left wall of the cavity to the upper left corner under the driving action of the fluid, with its relative position aL gradually increasing and reaching a maximum value at point B. During this period, the particle undergoes deceleration motion, and at point B, it reaches a minimum value due to the restriction of the upper wall. Then, during the time interval $28.6116 \leq \tau \leq 29.5881$ (B–C segment), aL gradually decreases as the particle moves along the top wall to the right. The velocity near the top wall is the highest, causing the particle's velocity magnitude to increase from a minimum value to a maximum value. As time increases to $29.5881 \leq \tau \leq 30.3693$ (C–D segment), the particle moves to the upper right corner of the cavity, aL increases to a maximum value (also the maximum value within one cycle), and the particle's velocity magnitude gradually decreases. Subsequently, during $30.3693 \leq \tau \leq 31.8341$ (D–E segment), the particle moves downward along the right wall of the cavity, aL decreases from a maximum value to a minimum value. At this time, the particle's velocity magnitude increases from a low peak value to a high peak value (also the maximum value within one cycle). During $31.8341 \leq \tau \leq 32.6153$ (E–F segment), the particle moves from the lower right corner to the lower left corner of the cavity, aL increases slowly, and its velocity magnitude shows a decreasing trend until it reaches the minimum value at point F. From point F to the next cycle's point A, the particle starts to turn from the lower left corner and moves to the vicinity of the left wall of the cavity, with its velocity magnitude increasing from a minimum value to the first maximum value of the cycle. In Fig. 8(b), it can be seen that the particle's orientation in the cavity flow is constantly changing, which also affects the particle flow system. Therefore, the particle's limit cycle is caused by the combined effects of inertial drive and wall constraints.

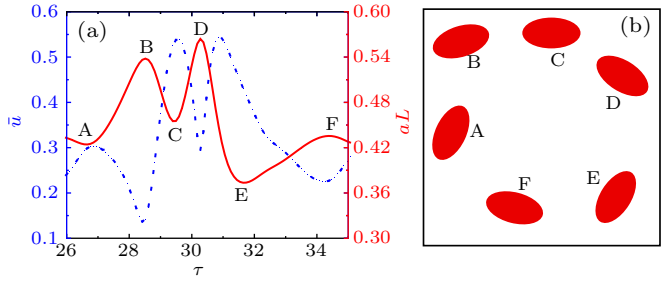


Fig. 8. Instantaneous curves of the distance between the particle centroid and the cavity center, and the velocity magnitude, as well as a schematic diagram of the relative position within a single period. (a) Instantaneous curves of the distance between particle centroid and cavity center, and velocity magnitude, (b) schematic diagram of relative position.

Figure 9 illustrates the contour of the tangential and normal forces acting on the boundary of the elliptical particle at six specific moments corresponding to Fig. 8. It is stipulated that the tangential force is positive in the clockwise direction and negative in the counterclockwise direction; the normal force is positive when directed from the boundary towards the exterior of the particle and negative when pointing towards the interior of the particle. From Fig. 9, one can observe the dynamic changes in the fluid forces acting on the particle surface at different moments. At different positions, it is evident that the fluid forces exerted on the particle surface exhibit significant heterogeneity in their tangential and normal distributions. The trajectory and turning of the particle are significantly influenced by this uneven force distribution. Specifically, the fluid forces create a complex force field on the particle surface, where the tangential forces cause the particle to accelerate or decelerate in the direction of fluid flow, and the normal forces cause the particle to deflect when encountering the cavity walls or other particles. The uneven distribution of these forces, coupled with the particle's own inertia, jointly determines the particle's motion characteristics in the fluid, including changes in its velocity and direction of motion.

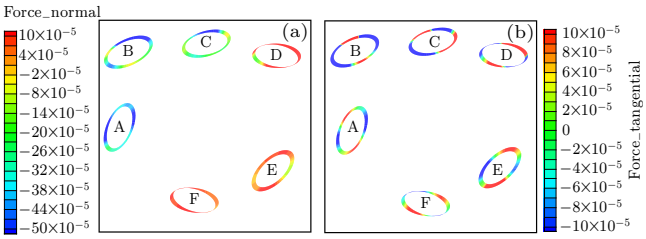


Fig. 9. Contour of (a) normal force and (b) tangential force acting on the boundary of elliptical particle at different moments.

Next, the impact of the particle's initial orientation, initial position, aspect ratio, and particle size on the particle's motion in the lid-driven cavity flow will be investigated.

4.2. Effect of initial orientation on the motion of particle

In this section, the effect of initial particle orientation on the motion of elliptical particles was investigated with initial orientation angles of $\theta = 0, \pi/4, \pi/2$. The Reynolds number in the square cavity, particle size, aspect ratio, and release position were kept consistent with the values used in Subsection 4.1. Figure 10 illustrates the trajectories of the centroid of elliptical particles with different initial orientations and the instantaneous curves of the velocity magnitude. It can be observed that the trajectories of the particles under the three initial orientations all converge to the same limit cycle, indicating that the initial orientation has a minimal impact on the final trajectory. Furthermore, the velocity magnitude of the particles is the same under different initial orientations, and the phase difference in time is very small, suggesting that the velocity magnitude of the particles is also not sensitive to the initial orientation. Therefore, it can be concluded that the initial orientation angle of the elliptical particles has no influence on the two stages of motion in this model.

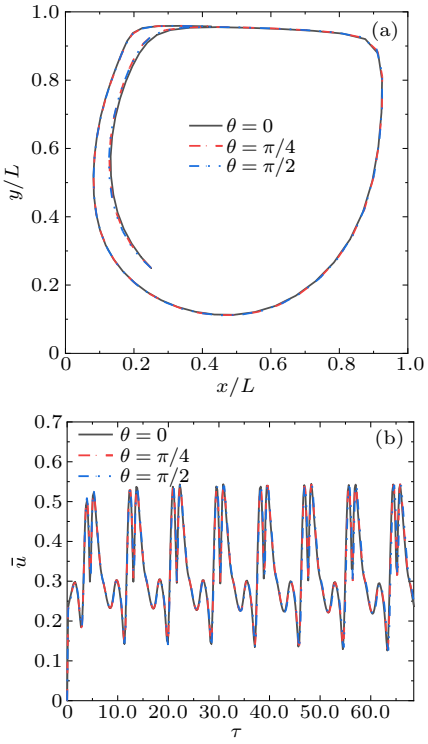


Fig. 10. Trajectories of particle motion and instantaneous velocity magnitude curves for different initial orientations. (a) Particle trajectories, (b) instantaneous velocity magnitude curves.

4.3. Effect of initial positions on the motion of particle

The fluid flow of the lid-driven cavity exhibits significant non-uniformity, implying that the flow characteristics at different locations may vary considerably. This non-uniformity of the flow can influence the motion of particles within the square cavity. In this section, three particle release positions were selected: I (0.25L, 0.25L), II (0.5L, 0.5L), III (0.75L,0.75L). The study investigated the impact of different particle release positions on the motion trajectories and velocity magnitude of the particles, while maintaining the same Reynolds number, particle size, aspect ratio, and initial orientation angle as those in Subsection 4.1. Figure 11 presents the motion trajectories of particles released at these three positions. It can be observed that initially, particles released at different positions undergo centrifugal motion. Subsequently, the motion of the particles is constrained by the boundaries of the cavity, ultimately reaching the same stable limit cycle.

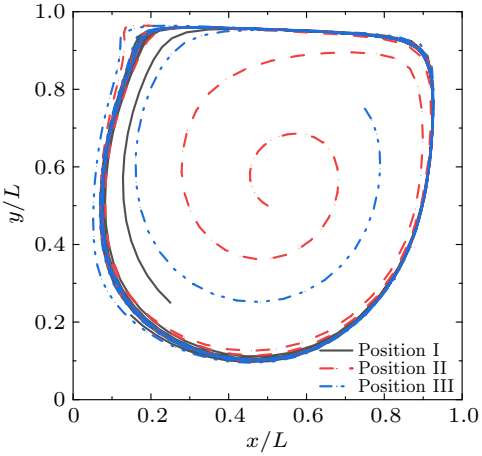


Fig. 11. Trajectories of particle motion for different initial release positions.

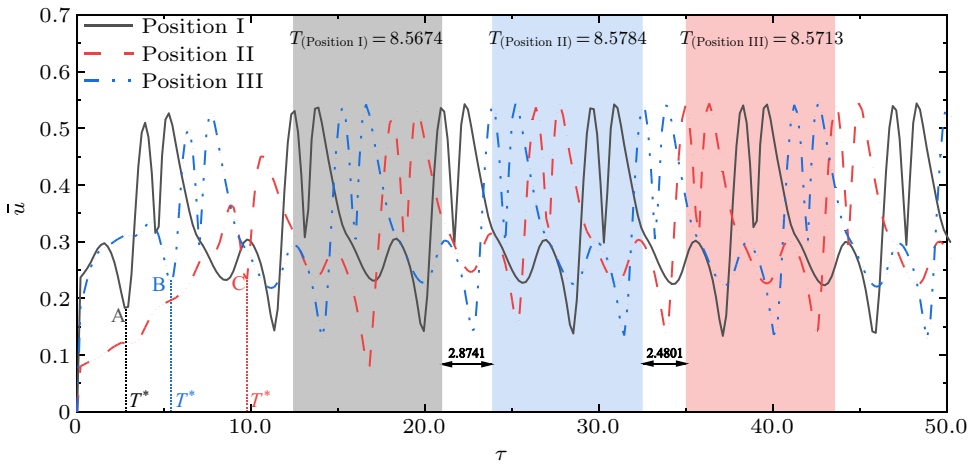


Fig. 12. Instantaneous velocity magnitude curves of particles for different initial release positions.

Figure 12 presents the instantaneous curves of the velocity magnitude for particles released at these three positions. It can be observed that due to the different initial positions, the phase of the velocity magnitude varies over time (as marked in the figure), but the magnitude and period of the velocity magnitude remain essentially constant after stabilization. The motion period of the particle released at position I (0.25L, 0.25L) is 8.5674, at position II (0.5L, 0.5L) is 8.5748, and at position III (0.75L, 0.75L) is 8.5713, which are close to the elliptical motion period $T = 8.5$ obtained in Subsection 4.1, which indicates that changing the initial release position affects the time required for the particle to complete the starting stage of motion, but has little impact on the periodic stage. Since particles released at different positions travel different distances to reach the limit cycle, the time required varies. Points A, B, and C correspond to the moments when the motion state of the

particles with three initial release positions enters the periodic stage (i.e., motion on the limit cycle), at which point the velocity magnitude instantaneous curve shows the first trough. Calculations show that the moments corresponding to points A, B, and C are $0.34T$, $1.16T$, and $0.66T$, respectively. The duration of the starting stage of motion for the particles is proportional to the distance from the initial release position to the limit cycle in all three cases.

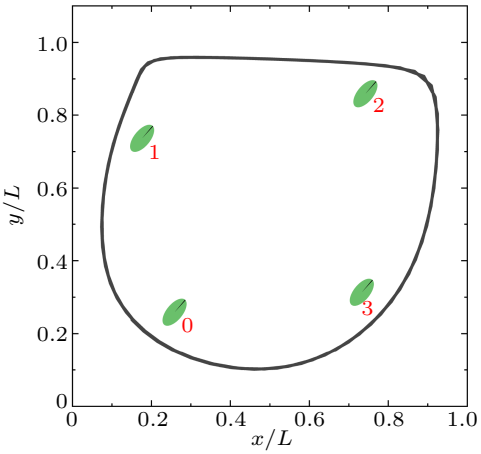


Fig. 13. Instantaneous velocity magnitude curves of particles for different initial release positions.

Subsequently, while maintaining the constant distance from the initial release position of the particle to the limit cycle, the variation in the time required for particles to reach the limit cycle from different release positions is studied. Initially, position I ($0.25L$, $0.25L$) is retained and redesignated as position 0, with the distance to the limit cycle calculated to be approximately $0.07L$. Subsequently, three new release positions are selected, designated as positions 1, 2, and 3, respectively. The new release positions are selected using the cavity's center as the origin, choosing one release point in each of the first, second, and fourth quadrants in order to remove the impact of the relative position within the square cavity. For specifics, refer to Fig. 13.

Table 1. Time to reach the limit cycle and phase difference in time for particles at different initial positions.

Positions	Time to reach the limit cycle	Phase difference in time with particle at position 1
	2.5897	1.1082
1	1.4815	–
2	7.9629	6.4814
3	12.2122	10.7307

Figure 14 presents a comparative analysis of the limit cycles of particle motion trajectories and the instantaneous velocity magnitude curves for the newly selected release positions. It can be observed that even when the initial position of the particle is equidistant from the limit cycle, there are still differences in temporal phase. Table 1 provides the time taken for particles to reach the limit cycle and the phase difference for four initial positions. It is evident that particles released in the upper left corner of the cavity reach the limit cycle earlier. This indicates that particles released in the upstream direction of the moving lid will reach the limit cycle more quickly. Furthermore, compared to particles released at position 0, those closer to the moving wall reach the limit cycle sooner.

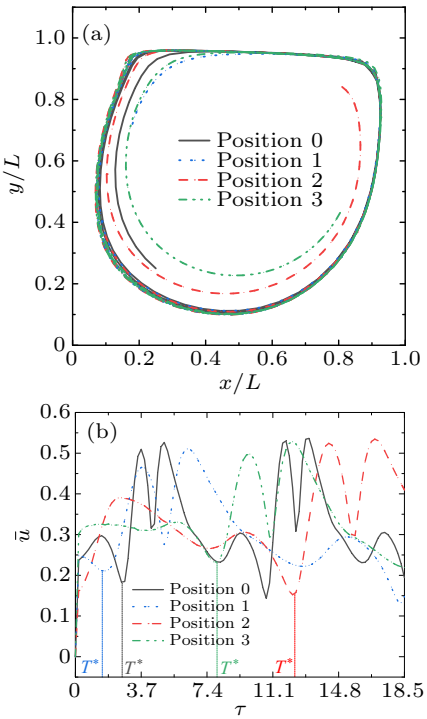


Fig. 14. Trajectories of particle motion and instantaneous velocity magnitude curves for different initial release positions. (a) Trajectories of particle motion. (b) Instantaneous velocity magnitude curves.

4.4. Effect of aspect ratios on the motion of particle

In this section, the aspect ratios of the elliptical particles φ are taken as 1, 2, and 3, respectively, to study the effect of aspect ratio on the motion of elliptical particles. The length of the semi-major axis a of the elliptical particles is kept constant, while the aspect ratio is altered by changing the length of the semi-minor axis b. The Reynolds number in the square cavity, particle size, initial orientation angle, and release position are maintained consistent with the values in Subsection 4.1. Figure 15 illustrates the motion trajectories of elliptical particles with different aspect ratios within the square cavity (when the aspect ratio is 1, the elliptical particle is essentially a circular particle). It can be observed that as the aspect ratio increases, the limit cycle of the particle trajectory deviates increasingly from a circular shape. To quantitatively describe the geometry of the limit cycle, the "roundness" $\varepsilon = (a/L)_{\min}/(a/L)_{\max}$ is calculated, which is defined as the ratio of the minimum distance to the maximum distance of the particle from the center of the cavity. A roundness closer to 1 indicates that the shape of the limit cycle is closer to a circle. For the elliptical particles with aspect ratios of 1, 2, and 3, the roundness values are $\varepsilon_1 = 0.611$, $\varepsilon_2 = 0.543$, $\varepsilon_3 = 0.498$, respectively, which is

consistent with the analysis in this section.

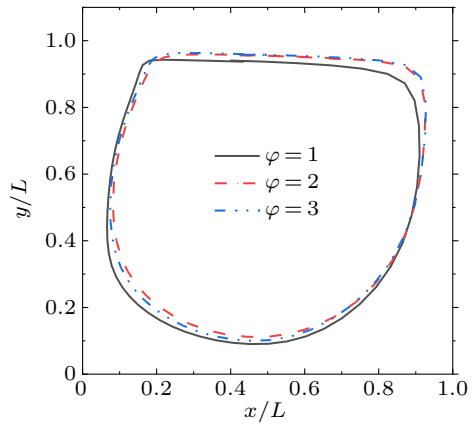


Fig. 15. Trajectories of particle motion for different aspect ratios.

Figure 16 presents the instantaneous velocity magnitude curves for particles with different aspect ratios. It can be observed that all three types of particles reach the first trough of their velocity magnitude at the same moment T^*, which corresponds to their arrival at the limit cycle of their trajectories. For aspect ratios of 1, 2, and 3, the motion periods are $T_{(\varphi=1)} = 9.9865$, $T_{(\varphi=2)} = 8.5674$, and $T_{(\varphi=3)} = 8.8160$, respectively. The phase differences in their motion periods are also marked in the figure. This indicates that changing the aspect ratio of the particle affects the periodic stage of motion, with a larger aspect ratio resulting in a shorter motion period, but has no effect on the starting stage. Hu[20] pointed out that when the aspect ratio of an elliptical particle changes, the fluid forces acting on the particle also change, which is reflected in the figure as different extreme values of the particle's velocity magnitude. It can be seen that as the aspect ratio increases, the velocity magnitude extreme values increase due to the more uneven distribution of hydrodynamic forces on the particle's surface, with the maximum velocity magnitude being $\bar{u}_1 = 0.499$, $\bar{u}_2 = 0.542$, and $\bar{u}_3 = 0.549$.

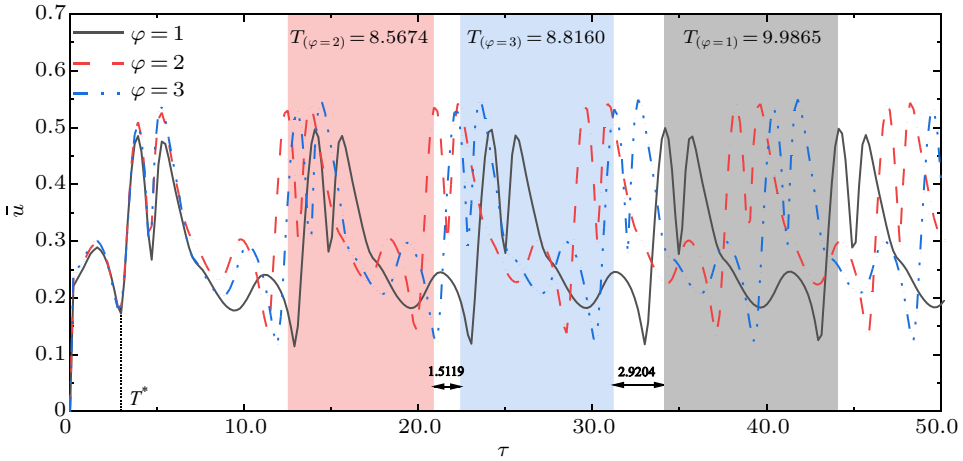


Fig. 16. Instantaneous velocity magnitude curves of particles with different aspect ratios.

4.5. Effect of size on the motion of particle

The size of the particle relative to the square cavity is of great importance. Within the cavity, the particle is subject to constraints imposed by the cavity boundaries. When the particle size is relatively small compared to the dimensions of the square cavity, the influence of the cavity boundaries on the particle's motion may be minimal. Conversely, as the ratio of particle size to cavity dimensions increases, the constraints imposed by the cavity boundaries become more pronounced, significantly affecting the particle's trajectory. In this section, the Reynolds number in the square cavity, particle aspect ratio, initial orientation angle, and release position are kept consistent with the values in Section 4.1. The relative sizes of the particles r are taken as 0.025, 0.05, and 0.1, respectively, to study the effect of particle size on the motion of elliptical particles. Figure 17 shows the motion trajectories of particles of these three sizes. It can be observed that the relative size of the particle significantly affects its motion within the cavity, and as the size increases, the limit cycle of the particle trajectory contracts towards the center of the cavity. This is due to the interplay between the centrifugal force acting on the particle and the restrictive effect of the square cavity boundaries. As the particle size increases, the boundary constraints become more pronounced, pushing the particle closer to the center of the square cavity. The motion trajectories of particles of different sizes can also be compared using the "roundness" ε. A larger value of roundness indicates that the trajectory loop is closer to the center of the cavity, experiencing less wall constraint effect, and thus the trajectory loop shape is closer to a circle. In Fig. 17, as the particle size increases, the roundness of the motion trajectory loops is $\varepsilon_{0.025} = 0.547$, $\varepsilon_{0.05} = 0.631$, and $\varepsilon_{0.1} = 0.661$, respectively.

Figure 18 presents the instantaneous velocity magnitude curves for particles of different sizes. It can be observed that particles of all three sizes reach the first trough of their velocity magnitude at the same moment T^*, which corresponds

to their arrival at the limit cycle of their trajectories. For particle sizes $r = 0.025$, 0.5 and 0.1, the motion periods are $T_{(r=0.025)} = 9.7650$, $T_{(r=0.05)} = 8.7588$, and $T_{(r=0.1)} = 8.5933$, respectively. This is because particles with larger relative sizes travel shorter distances, hence their motion periods are smaller. The phase differences in their motion periods are also marked in the figure. This indicates that changing the particle size only affects the periodic stage of motion and has little impact on the starting stage. Additionally, the greater the range of the velocity magnitude, the greater the change in velocity magnitude. As the particle size increases, the range of the velocity magnitude is 0.375, 0.305, and 0.205, respectively. This is because in the flow within the square cavity, the velocity change is greater closer to the wall. As the particle size increases, the wall's restrictive influence becomes more pronounced, and its motion trajectory moves further away from the cavity wall. Therefore, particles with larger relative sizes experience smaller changes in their velocity magnitude.

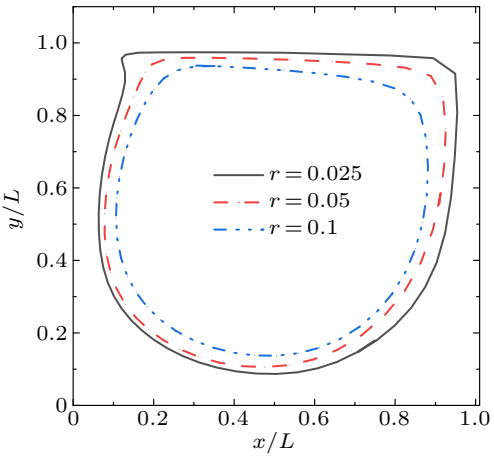


Fig. 17. Trajectories of particle motion for particles of different sizes.

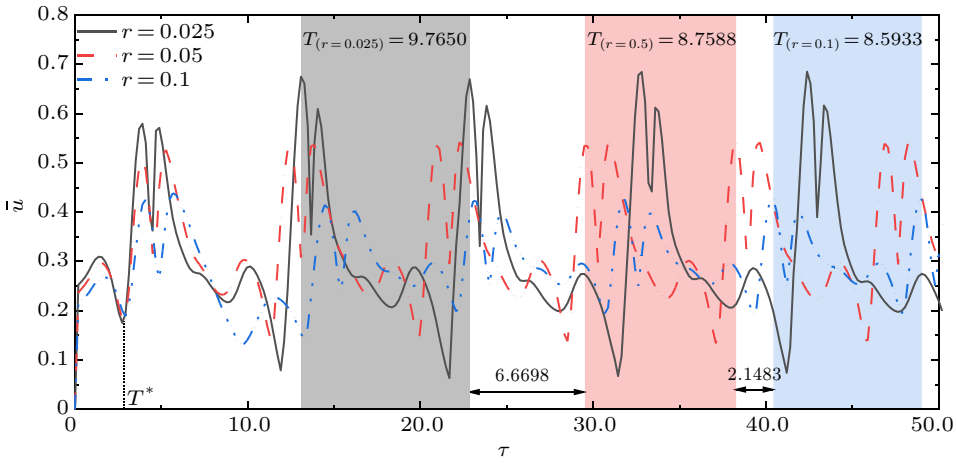


Fig. 18. Instantaneous velocity magnitude curves for particles of different sizes.

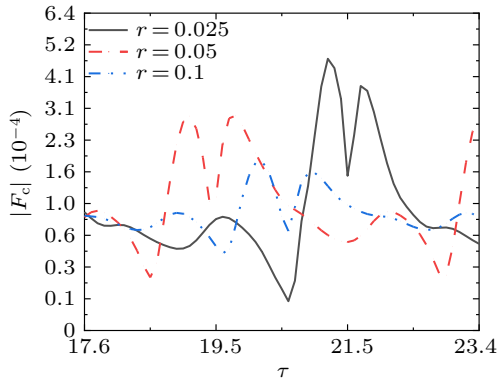


Fig. 19. Centrifugal forces experienced by particles of different sizes.

Figure 19 illustrates the centrifugal forces experienced by particles of different sizes. It can be observed that as the trajectory loop contracts towards the center of the square cavity, meaning the particle's motion trajectory is further away from the wall, the centrifugal force experienced by the particle decreases. The centrifugal forces experienced by the elliptical particles of the three sizes over one period are $\left|F_c^{0.025}\right| = 5.11 \times 10^{-4}$, $\left|F_c^{0.05}\right| = 2.70 \times 10^{-4}$, and $\left|F_c^{0.1}\right| = 1.45 \times 10^{-4}$, respectively. Consequently, this also leads to a smaller range of velocity magnitude for particles with larger sizes.

5. Conclusions

Based on the immersed boundary-lattice Boltzmann method, the motion of elliptical particles in a lid-driven square cavity flow was studied, and the research results are as follows:

(1) Elliptical neutrally buoyant particles moving in the lid-driven flow will first experience the starting stage, then reach the periodic stage, and maintain motion on a limit cycle, with both the motion and the physical parameters involved in the motion exhibiting distinct periodicity.

(2) Variation in the initial orientation of the particles alone has no impact on either stage of the particle motion.

(3) Variation in the initial release position of the particles results in different times required for the particles to reach the limit cycle, i.e., the starting stage of motion is different, reflected in the phase difference of the instantaneous velocity

curves. Particles released at positions I, II, and III reach the limit cycle in times of $0.34T$, $1.16T$, and $0.66T$, respectively, but have no effect on the periodic stage of particle motion.

(4) Further studies on the different initial release positions of particle found that factors such as releasing closer to the limit cycle, releasing in the upstream direction of the moving lid, and releasing in positions closer to the moving wall can enable particles to reach the limit cycle, i.e., the periodic stage, more quickly.

(5) Variation in the aspect ratio of the elliptical particles alone does not affect the starting stage of particle motion but does affect the periodic stage. Particles with a more flattened shape have motion trajectories that deviate more from a circular shape, and the maximum value of the combined velocity is also greater.

(6) For particles of different relative sizes, their starting stage of motion remains consistent, but their periodic stage is different. It can be considered that particles with larger relative sizes, due to the stronger restrictive effect of the wall, will cause the motion trajectory limit cycle to contract towards the center of the square cavity, thereby reducing the motion period.

(7) Variation in the initial orientation or initial release position of the particles does not change the periodic stage of particle motion because they are still the same particle, so it has no effect on the stable motion. Variation in the initial release position means changing the initial distance between the particle and the limit cycle, thus affecting the starting stage of particle motion. Variation in the aspect ratio or relative size of the particles means changing the properties of the particles, which leads to different expressions in their periodic stage. This can be summarized as follows: unless the physical parameters of the particle itself are changed, the periodic stage of particle motion will not change, and only changing the initial release position will affect the starting stage of particle motion.

References

[1] Krüger T, Holmes D and Coveney P V 2014 *Biomicrofluidics* **8** 054114
[2] Haddadi H, Naghsh-Nilchi H and Carlo D D 2018 *Biomicrofluidics* **12** 014112
[3] Whitesides G M 2006 *Nature* **442** 368
[4] You Z, Badalyan A, Yang Y, Bedrikovetsky P and Hand M 2019 *Geothermics* **77** 344
[5] Kosinski P, Kosinska A and Hoffmann A C 2009 *Powder Technol.* **191** 327
[6] Sidiq C A N and Attarzadeh N R M 2012 *Int. J. Eng. Sci.* **51** 90
[7] Xia Z H, Connington K W, Rapaka S, Yue P T, Feng J J and Chen S Y 2009 *J. Fluid Mech.* **625** 249
[8] Huang H B, Yang X and Lu X Y 2014 *Phys. Fluids* **26** 053302
[9] Qi D W and Luo L S 2003 *J. Fluid Mech.* **477** 201
[10] Tsorng S J, Capart H, Lai J S and Young D L 2005 *Exp. Fluids* **40** 314
[11] Puragliesi R, Dehbi A, Leriche E, Soldati A and Deville M O 2011 *Int. J. Heat Fluid Flow* **32** 915
[12] Bayareh M, Nourbakhsh A, Rouzbahani F I and Jouzaei V 2019 *SN Appl. Sci.* **1** 1040
[13] Yang F, Shao X S, Wang Y, Lu Y S and Cai X S 2021 *Eur. J. Mech. B Fluids* **86** 90
[14] Sun G, Zhang J H, Hu J J, Zhang M X, Pan H and Ye X P 2022 *Int. J. Mod. Phy. C* **34** 2350037
[15] Yang F, Dai M Y and Jin H 2024 *Processes* **12** 813
[16] Yang F, Yang H C, Yan Y H, Guo X Y, Dai R and Liu C Q 2017 *J. Mech. Sci. Technol.* **31** 3053
[17] Yang F, Jin H and Dai M Y 2024 *Chin. Phys. B* **33** 064702
[18] Chen W Y, Yang F, Yan Y H, Guo X Y, Dai R and Cai X S 2018 *J. Mech. Sci. Technol.* **32** 2637
[19] Hu J J, Sun D K, Mao S H, Wu H M, Yu S Y and Xu M S 2022 *J. Comput. Theor. Transp.* **51** 222
[20] Hu J J 2020 *Phys. Fluids* **32** 113304
[21] Zhang Y, Li C and Ye M 2023 *Phys. Fluids* **35** 123305
[22] Wang L, Li Z T, Wu S, Tao S, Zhang K, Bi J L and Lu G 2023 *J. Appl. Phys.* **134** 214701
[23] Ladd A J C 1994 *J. Fluid Mech.* **271** 285
[24] Mei R W, Luo L S, Lallemand P and d'Humières D 2006 *Comput. Fluids* **35** 855
[25] Inamuro T, Maeba K and Ogino F 2000 *Int. J. Multiphase Flow* **26** 1981
[26] Romanò F and Kuhlmann H C 2017 *Theor. Comput. Fluid Dyn.* **31** 427
[27] Gan H, Chang J Z, Feng J J and Hu H H 2003 *J. Fluid Mech.* **481** 385
[28] Yu Z, Shao X and Wachs A 2006 *J. Comput. Phys.* **217** 424
[29] Feng Z G and Michaelides E E 2009 *Int. J. Heat Mass Transfer* **52** 777
[30] Feng Z G and Michaelides E E 2008 *Phys. Fluids* **20** 040604
[31] Peskin C S 2002 *Acta Numer.* **11** 479
[32] Feng Z G and Michaelides E E 2005 *J. Comput. Phys.* **202** 20
[33] Shin S J and Sung H J 2011 *Phys. Rev. E* **83** 46321
[34] Sun D K, Jiang D, Xiang N, Chen K and Ni Z H 2013 *Chin. Phys. Lett.* **30** 74702
[35] Chen Y L 2014 *RSC Adv.* **4** 17908
[36] Kim B, Chang C B, Park S G and Sung H J 2015 *Int. J. Heat Fluid Flow* **54** 87
[37] Mukundakrishnan K, Hu H H and Ayyaswamy P S 2008 *J. Fluid Mech.* **599** 169
[38] Eshghinejadfard A and Thévenin D 2016 *Int. J. Heat Fluid Flow* **60** 31
[39] Zhang H, Shao Y J, Li K X and Hu Y 2017 *Powder Technol.* **314** 315
[40] Hu J J 2021 *Eur. J. Mech. B Fluids* **85** 124
[41] Guo Z L and Zheng C G 2008 *Int. J. Comput. Fluid D* **22** 465
[42] He X Y and Luo L S 1977 *J. Stat. Phys.* **88** 927
[43] Lu J H, Han H F, Shi B C and Guo Z L 2012 *Phys. Rev. E* **85** 016711
[44] Kang S K and Hassan Y A 2010 *Int. J. Numer. Methods Fluids* **66** 1132
[45] Niu X D, Shu C, Chew Y T and Peng Y 2006 *Phys. Lett. A* **354** 173
[46] Liu J, Huang C S, Chai Z H and Shi B C 2022 *Comput. Fluids* **233** 105246